

## Modeling of 3D Magnetostrictive Systems with Application to Galfenol and Terfenol-D Actuators

Marcelo J. Dapino<sup>1,a</sup>, Suryarghya Chakrabarti<sup>1,b</sup>

The Ohio State University, 201 W 19th Ave, Columbus, OH 43210 USA

<sup>a</sup>dapino.1@osu.edu, <sup>b</sup>chakrabarti.3@osu.edu

**Keywords:** magnetostriction, nonlinear dynamic model, constitutive modeling, eddy currents, finite element modeling

**Abstract.** This work presents a unified approach to model three dimensional magnetostrictive transducers. Generalized procedures are developed for incorporating nonlinear coupled constitutive behavior of magnetostrictive materials into an electro-magneto-mechanical finite element modeling framework. The finite element model is based on weak forms of Maxwell's equations for electromagnetics and Navier's equations for mechanical systems. An implicit time integration scheme is implemented to obtain nonlinear dynamic system responses. The model is implemented into a finite element (FE) solver and applied to two case studies, a Galfenol unimorph actuator and a magnetohydraulic Terfenol-D actuator for active engine mounts. Model results are compared with experiments, and parametric analyses are conducted which provide guidelines for optimization of actuator design.

### Introduction

Magnetostrictive materials exhibit coupling between the magnetic and mechanical energy domains. They undergo lattice deformation in response to applied magnetic fields and change their magnetic state when stressed. Short response times (in the millisecond range) combined with microstrain (or better) resolution make these materials suitable for precision sensing and actuation mechanisms [1].

Modeling the behavior of magnetostrictive systems is challenging as these systems exhibit multi-domain coupling both at the material and system level. Magnetostrictive transducer models aim at quantifying the relationship between transducer input and output parameters such as voltage, current, field, and displacement. This is done by formulating equations describing the coupled structural and magnetic dynamics of the system. Complete magnetostrictive transducer models use constitutive laws to couple three main components: voltage-field relationships, structural dynamics, and eddy currents. Description of voltage-field relationships and eddy currents requires information of complete transducer geometry and solution of Maxwell's equations in three dimensions (3D). Simpler, less accurate 1D and 2D transducer models have been formulated in which magnetic field is an input and magnetostatic operation is assumed to avoid solving Maxwell's equations.

Eddy current losses are significant when dynamic magnetostrictive devices are operated at high enough frequency. Eddy currents in a magnetostrictive driver can be incorporated into a constitutive law or, for cylindrical drivers, quantified by solving 1D magnetic field diffusion equations. Huang et al. [2] followed the former approach and coupled a lumped parameter vibratory model with the Jiles-Atherton equations extended to model eddy currents [3]. Sarawate and Dapino [4] implemented the second strategy by coupling a 1D magnetic field diffusion equation with a lumped-parameter model describing the structural dynamics using the Jiles-Atherton model. Evans [6] formulated an energy-averaged constitutive model in which a lumped-parameter vibratory model is coupled with a radial diffusion equation for magnetic fields. The nonlinear two-way coupled model was solved numerically using Newton-Raphson iterations.

Many of the early two dimensional finite element models for magnetostrictive devices are magnetostatic to avoid the complexities involved in modeling eddy currents. Benbouzid [7] formulated a 2D bidirectionally-coupled magnetostatic model formulated in terms of magnetic vector potentials in which Terfenol-D constitutive behavior is incorporated using surface splines. The coupled problem is solved through successive mechanical and magnetic finite element computations. Kannan and Dasgupta [8] presented a 2D magnetostatic model based on scalar magnetic potentials with bi-directionally coupled magnetomechanical relations, current induced magnetic fields, and electromagnetic body forces. A piecewise-linear solution process is used with constitutive laws incorporated in an incremental manner. Material model coefficients are obtained from bi-cubic spline fits to measurements. Zhou et al. [9] developed a dynamic finite element model of a unimorph actuator with one-way magnetomechanical coupling. Applied magnetic fields are computed explicitly in axial coordinates as a function of drive coil current. Constitutive nonlinearities are incorporated through the Zheng-Liu model [10]. The one-way coupled 3D model of Kim and Jung [11] describes force due to magnetostriction driving a coupled fluid-structural model for a sonar transducer. Magnetic fields are computed *a priori* and magnetostriction is described by fitting sixth-order polynomials to strain versus field curves.

The above models require as input externally applied fields or compute the magnetic field explicitly as a function of applied currents. The models described next aim at modeling the full coupling between the electromagnetic and mechanical boundary value problems. Ghosh et al. [12] described a magnetostatic finite element model for composite laminates incorporating magnetostrictive materials modeled using a linear anhysteretic constitutive law. A comparison between a one-way coupled and a two-way coupled implementation revealed significant differences emphasizing the need for fully-coupled models. Aparicio and Sosa [13] presented a 3D, fully-coupled finite element model based on vector magnetic potentials which does include dynamic effects; a very simple implementation was given. Slaughter [14] implemented a model for magnetostrictive transducers in the finite element software COMSOL by coupling the Structural Mechanics and AC/DC modules using linear piezomagnetic relations for the magnetostrictive material. Mudivartha et al. [15] used a fully-coupled, magnetostatic formulation to describe stress-induced flux density changes in Galfenol with no current-induced fields. An updated version of the model includes current induced fields but is still magnetostatic in nature [16]. Galfenol constitutive behavior is incorporated through look up tables generated *a priori* by running the Armstrong model [17] for a large number of induction and stress values. Although the Armstrong model is capable of describing 3D Galfenol behavior, look up tables were generated for 1D induction and stress inputs. Evans and Dapino [18] presented a fully-coupled dynamic model for 3D magnetostrictive transducers in which a vector magnetic potential is solved through a finite element formulation. The model simultaneously describes the effects of eddy currents, structural dynamics, and flux leakage on transducer performance, though displacement currents and electromagnetic body forces are neglected. Due to the restriction of COMSOL Multiphysics being unable to handle vectorized functions, linear constitutive behavior is assumed.

This work develops generalized methodologies to incorporate nonlinear constitutive laws in the finite element framework of Evans and Dapino [18]. The methods developed can be used for any arbitrary constitutive model as long as it can be analytically or numerically differentiated. The paper briefly reviews the finite element formulation followed by a description of the nonlinear dynamic system equations, a generalized procedure to integrate nonlinear coupled constitutive behavior within the framework, and the time integration methods implemented to obtain the nonlinear dynamic system responses. The final two sections deal with implementation of this unified model on a Galfenol unimorph and a Terfenol-D engine mount actuator.

## Finite Element Framework

The finite element model of Evans and Dapino [18] is based on weak form representation of the Maxwell's laws and Navier's equation. The resulting finite element model equations can be expressed as

$$\sum_{e=1}^{N^A} \left( \int_{\Delta} \mathbf{H}_e(\mathbf{B}_e, \mathbf{S}_e) \cdot \mathbf{C}_e \delta \mathbf{q}_e^A J_e d\Delta + \int_{\Delta} \sigma_e \mathbf{N}^A \frac{\partial \mathbf{q}_e^A}{\partial t} \cdot \mathbf{N}^A \delta \mathbf{q}_e^A J_e d\Delta \right) = \sum_{b=1}^{N_S^A} \int_{\Delta} \mathbf{H}_{T,b} \cdot \mathbf{N}^A \delta \mathbf{q}_b^A J_{b,S} d\Delta_S + \sum_{e=1}^{N^A} \int_{\Delta} \mathbf{J}_{s,e} \cdot \mathbf{N}^A \delta \mathbf{q}_e^A J_e d\Delta, \quad (1)$$

$$\sum_{e=1}^{N^u} \left( \int_{\Delta} \mathbf{T}_e(\mathbf{B}_e, \mathbf{S}_e) \cdot \mathbf{G}_e \delta \mathbf{q}_e^u J_e d\Delta + \int_{\Delta} \rho_e \mathbf{N}^u \frac{\partial^2 \mathbf{q}_e^u}{\partial t^2} \cdot \mathbf{N}^u \delta \mathbf{q}_e^u J_e d\Delta + \int_{\Delta} c_e \mathbf{N}^u \frac{\partial \mathbf{q}_e^u}{\partial t} \cdot \mathbf{N}^u \delta \mathbf{q}_e^u J_e d\Delta \right) = \sum_{b=1}^{N_S^u} \int_{\Delta_S} \mathbf{t}_b \cdot \mathbf{N}^u \delta \mathbf{q}_b^u J_{b,S} d\Delta_S, \quad (2)$$

where  $e$  denotes the element number over which the quantities are evaluated. The vectors  $\mathbf{H}_e$ ,  $\mathbf{B}_e$ ,  $\mathbf{S}_e$ ,  $\mathbf{T}_e$  are the magnetic field, magnetic flux density, strain, and stress in element  $e$ ;  $\mathbf{C}_e$  and  $\mathbf{G}_e$  are matrix representations of the curl and gradient operator. Within every element the vector magnetic potential  $\mathbf{A}_e$  and the mechanical displacements  $\mathbf{u}_e$  are interpolated from the corresponding nodal degrees of freedom  $\mathbf{q}_e^A$  and  $\mathbf{q}_e^u$  using the shape function matrices  $\mathbf{N}^A$  and  $\mathbf{N}^u$ , respectively. Variables  $N^A$  and  $N^u$  are the number of elements in the magnetic and mechanical domains, respectively. The subscript  $b$  refers to the element number on the boundary. The number of elements on the boundary in which a magnetic field is applied is  $N_S^A$  and the number of boundary elements to which a traction is applied is  $N_S^u$ . The integral  $\int_{\Delta} J_e d\Delta$  is calculated over the element's volume in natural coordinates; the integral  $\int_{\Delta_S} J_{b,S} d\Delta_S$  gives the surface area of the element's face on the boundary.

## Nonlinear Dynamic System Equations

The nonlinear dynamic system equations can be obtained by equating the coefficients of the virtual quantities in (1) and (2),

$$\mathbf{M}\ddot{\mathbf{U}} + \mathbf{D}\dot{\mathbf{U}} = \mathbf{R}(t) - \mathbf{F}(\mathbf{U}, t), \quad (3)$$

where the mass matrix  $\mathbf{M}$ , damping matrix  $\mathbf{D}$ , and state vector  $\mathbf{U}$  are of the form

$$\mathbf{M} = \begin{bmatrix} \mathbf{0} & \mathbf{0} \\ \mathbf{0} & \mathbf{M}^u \end{bmatrix}, \quad \mathbf{D} = \begin{bmatrix} \mathbf{D}^A & \mathbf{0} \\ \mathbf{0} & \mathbf{D}^u \end{bmatrix}, \quad \mathbf{U} = \begin{pmatrix} \mathbf{Q}^A \\ \mathbf{Q}^u \end{pmatrix}. \quad (4)$$

The vector of externally applied forces  $\mathbf{R}(t)$  and the internal nodal force vector  $\mathbf{F}(\mathbf{U}, t)$  are

$$\mathbf{R} = \begin{pmatrix} \mathbf{R}^A \\ \mathbf{R}^u \end{pmatrix}, \quad \mathbf{F} = \begin{pmatrix} \mathbf{F}^A \\ \mathbf{F}^u \end{pmatrix}, \quad (5)$$

where  $\mathbf{R}^A$  includes contributions from coil source current density and externally imposed tangential fields, and  $\mathbf{R}^u$  includes contributions from surface tractions,

$$\mathbf{R}^u = \sum_{b=1}^{N_S^u} \int_{\Delta_S} (\mathbf{N}^u)^T \mathbf{t}_b J_{b,S} d\Delta_S, \quad (6)$$

$$\mathbf{R}^A = \sum_{b=1}^{N_S^A} \int_{\Delta_S} (\mathbf{N}^A)^T \mathbf{H}_T J_{b,S} d\Delta_S + \sum_{e=1}^{N^A} \int_{\Delta} (\mathbf{N}^A)^T \mathbf{J}_{s,e} J_e d\Delta. \quad (7)$$

Similarly,  $\mathbf{F}^A$  and  $\mathbf{F}^u$  include contributions from fields and stresses acting on the elements,

$$\mathbf{F}^A = \sum_{e=1}^{N^A} \int_{\Delta} \mathbf{C}_e^T \mathbf{H}_e(\mathbf{B}_e, \mathbf{S}_e) J_e d\Delta, \quad (8)$$

$$\mathbf{F}^u = \sum_{e=1}^{N^u} \int_{\Delta} \mathbf{G}_e^T \mathbf{T}_e(\mathbf{B}_e, \mathbf{S}_e) J_e d\Delta. \quad (9)$$

The tangent stiffness matrix is obtained by differentiating  $\mathbf{F}$  with respect to  $\mathbf{U}$ ,

$$\mathbf{K} = \begin{bmatrix} \partial \mathbf{F}^A / \partial \mathbf{Q}^A & \partial \mathbf{F}^A / \partial \mathbf{Q}^u \\ \partial \mathbf{F}^u / \partial \mathbf{Q}^A & \partial \mathbf{F}^u / \partial \mathbf{Q}^u \end{bmatrix}, \quad (10)$$

where

$$\frac{\partial \mathbf{F}^A}{\partial \mathbf{Q}^A} = \sum_{e=1}^{N^A} \int_{\Delta} \mathbf{C}_e^T \frac{\partial \mathbf{H}_e}{\partial \mathbf{B}_e} \mathbf{C}_e J_e d\Delta, \quad (11)$$

$$\frac{\partial \mathbf{F}^A}{\partial \mathbf{Q}^u} = \sum_{e=1}^{N^u} \int_{\Delta} \mathbf{C}_e^T \frac{\partial \mathbf{H}_e}{\partial \mathbf{S}_e} \mathbf{G}_e J_e d\Delta, \quad (12)$$

$$\frac{\partial \mathbf{F}^u}{\partial \mathbf{Q}^A} = \sum_{e=1}^{N^u} \int_{\Delta} \mathbf{G}_e^T \frac{\partial \mathbf{T}_e}{\partial \mathbf{B}_e} \mathbf{C}_e J_e d\Delta, \quad (13)$$

$$\frac{\partial \mathbf{F}^u}{\partial \mathbf{Q}^u} = \sum_{e=1}^{N^u} \int_{\Delta} \mathbf{G}_e^T \frac{\partial \mathbf{T}_e}{\partial \mathbf{S}_e} \mathbf{G}_e J_e d\Delta. \quad (14)$$

Thus, determination of the internal nodal force vector requires computation of stress and field given strain and induction while computation of the tangent stiffness matrix requires determination of the derivatives  $\partial \mathbf{H}_e / \partial \mathbf{B}_e$ ,  $\partial \mathbf{H}_e / \partial \mathbf{S}_e$ ,  $\partial \mathbf{T}_e / \partial \mathbf{B}_e$ ,  $\partial \mathbf{T}_e / \partial \mathbf{S}_e$  each of which need to be supplied by the constitutive law. The next section briefly reviews prior techniques to incorporate magnetostrictive material constitutive behavior in finite element models and details a generalized procedure for integrating coupled constitutive laws in the finite element framework described earlier.

## Incorporation of Nonlinear Constitutive Laws

Incorporation of nonlinear constitutive behavior poses a significant challenge in the formulation of coupled finite element models for magnetostrictive systems. The most common method to describe magnetostrictive material behavior has been by obtaining polynomial fits to data. For example, Benbouzid et al. [19] used surface splines to fit experimental data while Kannan and Dasgupta [8] used constitutive relations in an incremental form with coefficients obtained from bi-cubic spline fits to measurements. Kim et al. [11] used sixth order polynomials to fit the strain-field behavior with a different set of coefficients for each preload condition. The use of spline functions has the advantages of easy differentiability and implementation for 1D cases. However, the use of splines for 3D material behavior is complex as it requires 3D measurements along with bulky splines with 9 components (3 for field and 6 for stress) that are fitted to the measurements. Graham et al. [16] implemented Galfenol constitutive behavior through look-up tables generated *a priori* using the Armstrong model for a large number of induction and stress values. Although the Armstrong model is three dimensional, look-up tables were generated for 1D induction and stress inputs. As is the case with splines, extension to a full 3D version will add significant complexity because it will require generation of bulky tables with 9 inputs and 9 outputs. For these reasons, using an implicit constitutive law is beneficial for 3D boundary value problems.

Most available constitutive laws take magnetic field ( $\mathbf{H}$ ) and stress ( $\mathbf{T}$ ) as inputs and compute flux density  $\mathbf{B}$  and strain ( $\mathbf{S}$ ) as outputs,

$$\mathbf{B} = \mathbf{B}(\mathbf{H}, \mathbf{T}), \quad \mathbf{S} = \mathbf{S}(\mathbf{H}, \mathbf{T}). \quad (15)$$

These models can be analytically or numerically differentiated to obtain the matrix of derivatives (or the material Jacobian matrix), which has the form

$$\mathcal{J} = \begin{bmatrix} \boldsymbol{\mu} = \partial \mathbf{B} / \partial \mathbf{H}(\mathbf{H}_0, \mathbf{T}_0) & \mathbf{d} = \partial \mathbf{B} / \partial \mathbf{T}(\mathbf{H}_0, \mathbf{T}_0) \\ \mathbf{d}^T = \partial \mathbf{S} / \partial \mathbf{H}(\mathbf{H}_0, \mathbf{T}_0) & \mathbf{s} = \partial \mathbf{S} / \partial \mathbf{T}(\mathbf{H}_0, \mathbf{T}_0) \end{bmatrix}. \quad (16)$$

The material Jacobian matrix inverse can be used not only for assembling the stiffness matrix but also for inversion of the constitutive model using Newton's method. Computation of the Jacobian matrix on every Newton-Raphson iteration requires significant computational effort causing large solution times. Use of Quasi-Newton methods to invert the constitutive law eliminates the need to compute the material Jacobian at every iteration. Further, the Jacobian inverse can be approximated during the inversion process and stored to be used during the stiffness matrix assembly.

## Time Integration

Once the constitutive model has been integrated into the framework such that the system matrices can be computed, the last step in obtaining a dynamic solution is to select a suitable time-stepping algorithm. Bathe [20] suggested various explicit and implicit time-integration algorithms for nonlinear structural problems of similar form. In this case explicit methods are ruled out since the mass matrix is singular. An implicit scheme based on the trapezoidal rule is implemented, combined with equilibrium iterations. At the  $k^{th}$  iteration the system equations can be written as

$$\mathbf{M}^{t+\Delta t} \ddot{\mathbf{U}}^{(k)} + \mathbf{D}^{t+\Delta t} \dot{\mathbf{U}}^{(k)} + {}^{t+\Delta t}\mathbf{K}^{(k-1)} \Delta \mathbf{U}^{(k)} = {}^{t+\Delta t}\mathbf{R} - {}^{t+\Delta t}\mathbf{F}^{(k-1)}, \quad (17)$$

$${}^{t+\Delta t}\mathbf{U}^{(k)} = {}^{t+\Delta t}\mathbf{U}^{(k-1)} + \Delta \mathbf{U}^{(k)}. \quad (18)$$

According to the trapezoidal rule of time integration, the following assumptions are used:

$${}^{t+\Delta t}\mathbf{U} = {}^t\mathbf{U} + \frac{\Delta t}{2} ({}^t\dot{\mathbf{U}} + {}^{t+\Delta t}\dot{\mathbf{U}}), \quad (19)$$

$${}^{t+\Delta t}\dot{\mathbf{U}} = {}^t\dot{\mathbf{U}} + \frac{\Delta t}{2} ({}^t\ddot{\mathbf{U}} + {}^{t+\Delta t}\ddot{\mathbf{U}}). \quad (20)$$

The vectors  $\ddot{\mathbf{U}}^{(k)}$  and  $\dot{\mathbf{U}}^{(k)}$  can be written using (18) to (20) as

$${}^{t+\Delta t}\ddot{\mathbf{U}}^{(k)} = \frac{4}{\Delta t^2} ({}^{t+\Delta t}\mathbf{U}^{(k-1)} - {}^t\mathbf{U} + \Delta\mathbf{U}^{(k)}) - \frac{4}{\Delta t} {}^t\dot{\mathbf{U}} - {}^t\ddot{\mathbf{U}}, \quad (21)$$

$${}^{t+\Delta t}\dot{\mathbf{U}}^{(k)} = \frac{2}{\Delta t} ({}^{t+\Delta t}\mathbf{U}^{(k-1)} - {}^t\mathbf{U} + \Delta\mathbf{U}^{(k)}) - {}^t\dot{\mathbf{U}}. \quad (22)$$

Substitution into (17) yields the equation of motion for the system,

$$\left[ {}^{t+\Delta t}\mathbf{K}^{(k-1)} + \frac{4\mathbf{M}}{\Delta t^2} + \frac{2\mathbf{D}}{\Delta t} \right] \Delta\mathbf{U}^{(k)} = {}^{t+\Delta t}\mathbf{R} - \mathbf{M} \left[ \frac{4}{\Delta t^2} ({}^{t+\Delta t}\mathbf{U}^{(k-1)} - {}^t\mathbf{U}) - \frac{4}{\Delta t} {}^t\dot{\mathbf{U}} - {}^t\ddot{\mathbf{U}} \right] - \mathbf{D} \left[ \frac{2}{\Delta t} ({}^{t+\Delta t}\mathbf{U}^{(k-1)} - {}^t\mathbf{U}) - {}^t\dot{\mathbf{U}} \right] - {}^{t+\Delta t}\mathbf{F}^{(k-1)}. \quad (23)$$

The starting values for the internal force and state vector are considered to be same as the corresponding final values of the previous time step,

$${}^{t+\Delta t}\mathbf{F}^{(0)} = {}^t\mathbf{F}, \quad {}^{t+\Delta t}\mathbf{U}^{(0)} = {}^t\mathbf{U}. \quad (24)$$

The convergence criteria used in this work are based on energy and norm of the out-of-balance load vector [20]. Mathematically, these criteria can be written as

$$\frac{\| {}^{t+\Delta t}\mathbf{R} - {}^{t+\Delta t}\mathbf{F}^{(k-1)} - \mathbf{M} {}^{t+\Delta t}\ddot{\mathbf{U}}^{(k-1)} - \mathbf{D} {}^{t+\Delta t}\dot{\mathbf{U}}^{(k-1)} \|}{RNORM} \leq RTOL, \quad (25)$$

$$\frac{\Delta\mathbf{U}^{(k)} \cdot ({}^{t+\Delta t}\mathbf{R} - {}^{t+\Delta t}\mathbf{F}^{(k-1)} - \mathbf{M} {}^{t+\Delta t}\ddot{\mathbf{U}}^{(k-1)} - \mathbf{D} {}^{t+\Delta t}\dot{\mathbf{U}}^{(k-1)})}{\Delta\mathbf{U}^{(1)} \cdot ({}^{t+\Delta t}\mathbf{R} - {}^t\mathbf{F} - \mathbf{M} {}^t\ddot{\mathbf{U}} - \mathbf{D} {}^t\dot{\mathbf{U}})} \leq ETOL. \quad (26)$$

The mass and damping matrix are state-independent and hence are assembled only once for the entire simulation. The internal nodal force vector  $\mathbf{F}$  and the tangential stiffness matrix  $\mathbf{K}$  are assembled in every iteration as they are state-dependent. Thus, efficient computation of  $\mathbf{F}$  and  $\mathbf{K}$  is critical to the performance of the model. The next two sections show the application of the developed unified methodologies to Galfenol and Terfenol-D actuators.

## Galfenol Transducers

Magnetostrictive iron-gallium alloys (Galfenol) possess structural-grade mechanical properties in addition to exhibiting moderate magnetostriction. Galfenol can be machined, rolled, welded, and extruded into intricate shapes, thus enabling magnetostrictive transducers with 3D functionality. Galfenol is capable of withstanding tension, compression, and shock loads making it uniquely well-suited for application in load-bearing sensors and actuators. This section deals with integrating a nonlinear energy-averaged constitutive law for Galfenol with the finite element framework of Evans and Dapino [18] using the generalized procedures described in the previous section. The full nonlinear coupling between the electrical, magnetic, and mechanical domains in Galfenol systems is described.

**Discrete energy-averaged constitutive model for Galfenol.** The energy-averaged models describe macroscopic material response based on an energy weighted summation of contributions from domains aligned along different orientations. Mathematically this is represented as

$$\mathbf{M} = M_s \sum_{k=1}^r \xi^k \mathbf{m}^k, \quad (27)$$

$$\mathbf{S} = \mathbf{sT} + \sum_{k=1}^r \xi^k \mathbf{S}_m^k, \quad (28)$$

where  $\mathbf{M}$  and  $\mathbf{S}$  are the macroscopic magnetization and strain,  $M_s$  is the saturation magnetization,  $\mathbf{m}^k$  is the domain orientation vector and  $\xi^k$  is the volume fraction of domains aligned along orientation  $\mathbf{m}^k$ . The vector  $\mathbf{S}_m^k$  represents the strain as a function of the domain orientation. For a cubic material it is given by

$$\mathbf{S}_m^k = \begin{pmatrix} (3/2)\lambda_{100} (m_1^k)^2 \\ (3/2)\lambda_{100} (m_2^k)^2 \\ (3/2)\lambda_{100} (m_3^k)^2 \\ 3\lambda_{111}m_1^k m_2^k \\ 3\lambda_{111}m_2^k m_3^k \\ 3\lambda_{111}m_3^k m_1^k \end{pmatrix}. \quad (29)$$

The type and number of possible domain orientation vectors  $\mathbf{m}^k$  greatly affects the accuracy and efficiency of the model. With homogeneously distributed fixed orientations (as in Armstrong's model [17]), obtaining high accuracy requires a large number of possible orientations to be considered which results in significant computational load. Atulasimha et al. [21] improved the efficiency of these models by tracking the volume fractions of domains aligned along ninety eight fixed orientations. To preserve accuracy along with computational efficiency, Evans and Dapino [22] restricted the number of possible orientations to six by considering only the directions which minimize an energy function defined locally around each easy axis.

The total free energy of a domain close to the  $k^{th}$  easy axis  $\mathbf{c}^k$  is formulated as the sum of local anisotropy energy, magnetomechanical coupling energy, and Zeeman energy as

$$G^k = \frac{1}{2}K^k |\mathbf{m}^k - \mathbf{c}^k|^2 - \mathbf{S}_m^k \cdot \mathbf{T} - \mu_0 M_s \mathbf{m}^k \cdot \mathbf{H}. \quad (30)$$

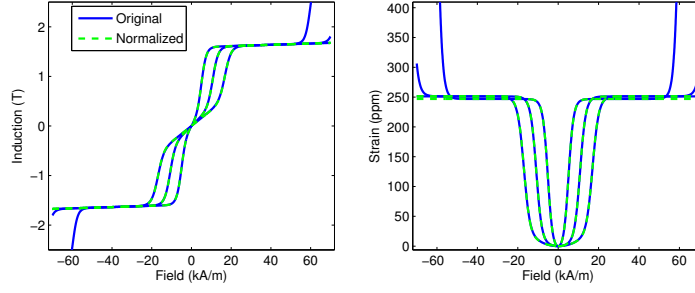


Fig. 1: Comparison of model outputs with and without normalizing  $\mathbf{m}^k$ . Simulations run at constant prestresses of 20, 50 and 80 MPa.

Minimization of the energy function and linearization of the unity norm constraint on the orientation vectors ( $\mathbf{m}^k \cdot \mathbf{m}^k = 1 \approx \mathbf{c}^k \cdot \mathbf{m}^k = 1$ ) yields the following analytical expression for the  $k^{th}$  local minimum

$$\mathbf{m}^k = (\mathbf{K}^k)^{-1} \left[ \mathbf{B}^k + \frac{1 - \mathbf{c}^k \cdot (\mathbf{K}^k)^{-1} \mathbf{B}^k}{\mathbf{c}^k \cdot (\mathbf{K}^k)^{-1} \mathbf{c}^k} \mathbf{c}^k \right], \quad (31)$$

where the magnetic stiffness matrix  $\mathbf{K}^k$  and force vector  $\mathbf{B}^k$  are

$$\mathbf{K}^k = \begin{bmatrix} K^k - 3\lambda_{100}T_1 & -3\lambda_{111}T_4 & -3\lambda_{111}T_6 \\ -3\lambda_{111}T_4 & K^k - 3\lambda_{100}T_2 & -3\lambda_{111}T_5 \\ -3\lambda_{111}T_6 & -3\lambda_{111}T_5 & K^k - 3\lambda_{100}T_3 \end{bmatrix}, \quad (32)$$

$$\mathbf{B}^k = [c_1^k K^k + \mu_0 M_s H_1 \quad c_2^k K^k + \mu_0 M_s H_2 \quad c_3^k K^k + \mu_0 M_s H_2]^T. \quad (33)$$

The anhysteretic volume fractions are calculated using Boltzmann-type averaging,

$$\xi_{an}^k = \frac{\exp(-G^k/\Omega)}{\sum_{j=1}^r \exp(-G^j/\Omega)}, \quad (34)$$

where  $\Omega$  is an averaging factor. As a result of linearization of the unity norm constraint, at very high fields well in the saturation regime, the norm of  $\mathbf{m}^k$  can become much greater than unity thus yielding unphysical magnetization and strain calculations. To circumvent this issue,  $\mathbf{m}^k$  is divided by its norm to maintain stability in the model. Figure 1 shows how normalization of the domain orientation vectors yields stability at saturation fields and at the same time preserves the accuracy of the original model at the non-saturation zones.

An advantage of having analytical expressions for the minimum energy orientations as opposed to an iterative numerical root finding algorithm is that the constitutive law can be analytically differentiated to obtain the material Jacobian matrix. Details of the Jacobian computation can be found in Chakrabarti and Dapino [23].

**Case study: Galfenol unimorph actuator.** The finite element model is validated using the Galfenol unimorph actuator shown in Figure 2(a). The actuator consists of a composite beam having a Galfenol layer bonded to a brass substrate, a drive coil, and steel flux return components. The system is excited by applying a voltage input to the coil; the vertical tip deflection of the beam is measured with a laser displacement sensor. Figure 2(b) shows the mesh geometry used for finite element calculations. The lower surface of the stainless steel piece to which the beam is clamped is mechanically fixed ( $\mathbf{u} = 0$ ) to remove rigid body modes. The actuator is surrounded by a sufficiently large air volume such that the magnetic potential is negligible at its outer boundaries,  $\mathbf{A} = 0$ .

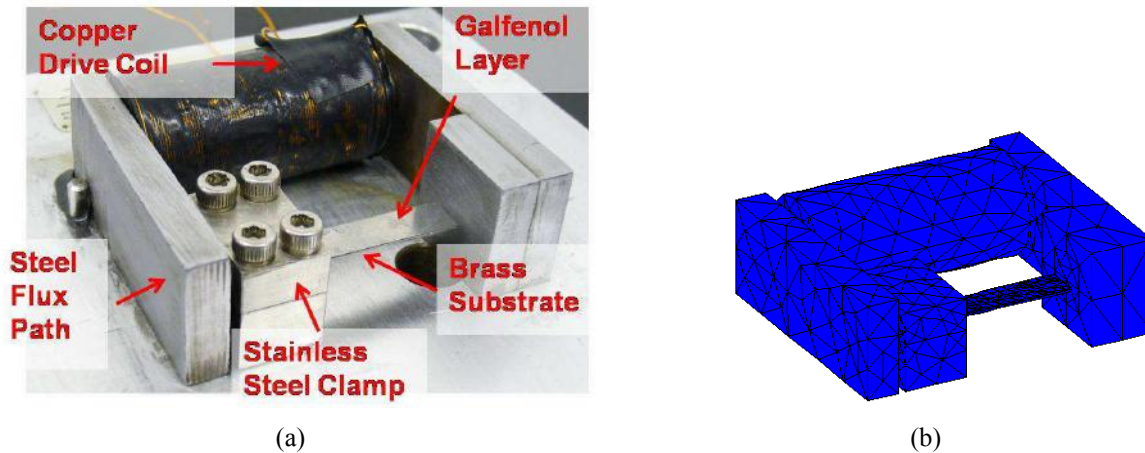


Fig. 2: Galfenol unimorph actuator used for model validation, (a) actuator configuration, and (b) finite element mesh.

To validate the nonlinear dynamic solution procedure, harmonic excitations ranging from 10 Hz to 200 Hz are applied to the system in the form  $V(t) = -V_{bias} + V_0(1 - \cos(\omega_{dr}t))$ , where  $\omega_{dr}$  is the excitation frequency and the finite element model is run for the first few cycles. In order to obtain appreciable displacement response from the beam at higher frequencies, a negative bias voltage ( $V_{bias}$ ) is applied first before applying the harmonic signal. This ensures that the effective bias point of the cyclic signal is in the burst region. In the model the bias point is obtained in similar fashion by applying the bias voltage smoothed using a hyperbolic tangent function for ease of convergence. Figure 3 shows the transient response of the transducer for harmonic inputs at 10, 50, 100, and 200 Hz. The model shows good correlation with the experiments particularly for the tip deflection response. An interesting outcome of nonlinear Galfenol behavior can be seen where the quadratic nonlinearity of the magnetostrictive strain at zero field causes frequency doubling in the tip deflection response.

### Terfenol-D Transducers

Magnetostrictive Terfenol-D ( $\text{Tb}_{0.7}\text{Dy}_{0.3}\text{Fe}_2$ ) is attractive for practical actuators due to its large magnetostriction (1600 ppm) and moderate saturation fields (200 kA/m). Due to its poor machinability, Terfenol-D is mostly available in 1D geometries like cylindrical rods. As a result, most Terfenol-D transducers are axisymmetric with the permanent magnet and flux return components concentric with the Terfenol-D driver. Thus, the 3D finite element model is reduced to a 2D axisymmetric form. The basic formulation is combined with a fully-coupled energy-averaged model for Terfenol-D. It is then used to model the steady state dynamic response of a Terfenol-D engine mount actuator.

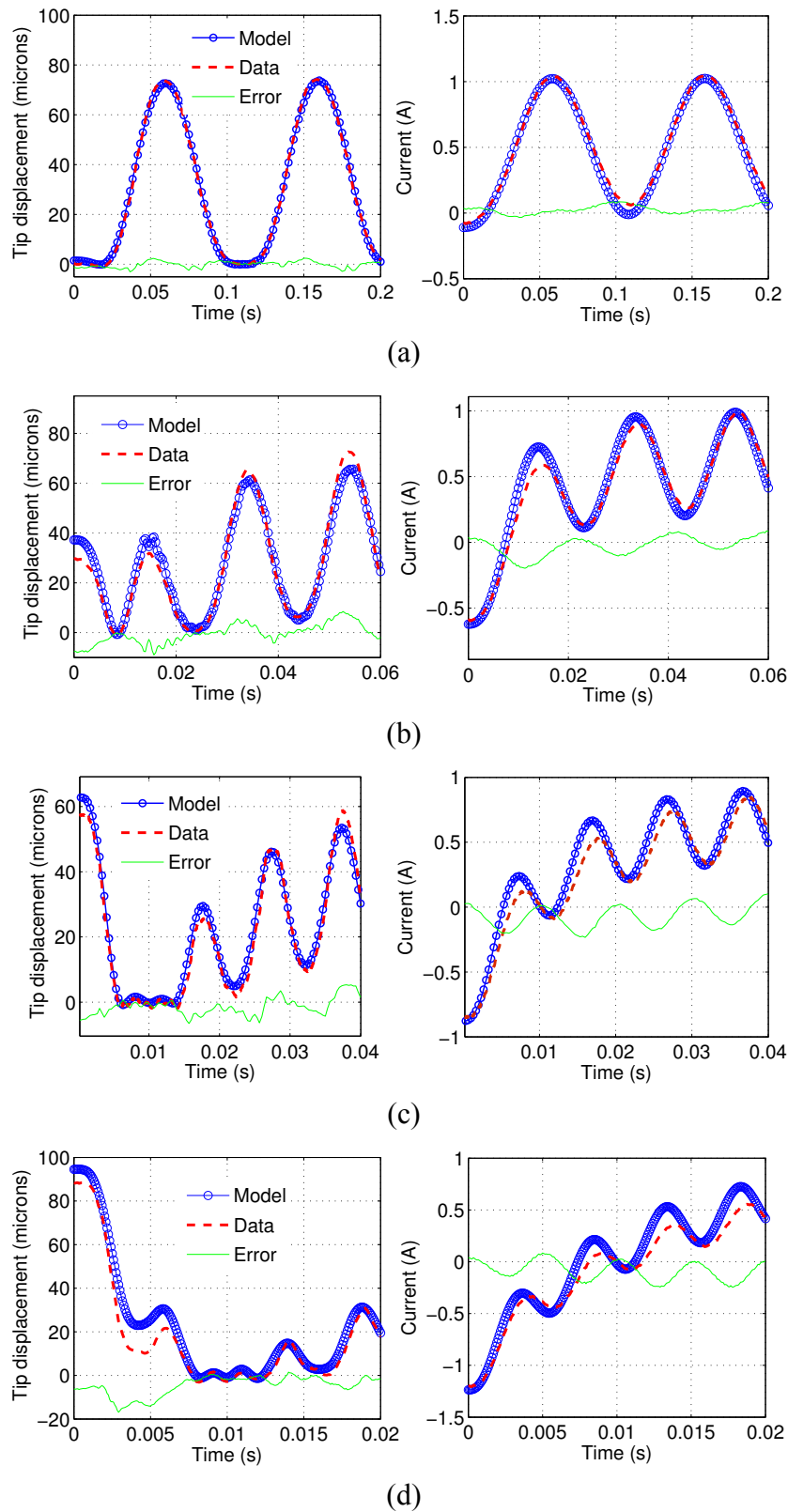


Fig. 3: From top to bottom, tip displacement and current drawn under harmonic excitation of: (a) 10 Hz, (b) 50 Hz, (c) 100 Hz, and (d) 200 Hz, respectively.

**Axisymmetric finite element formulation.** Terfenol-D transducers are commonly built with the cylindrical magnetostrictive rod at the core with concentric components like coil, permanent magnets, and flux return. An axisymmetric formulation can efficiently model such transducers without sacrificing accuracy. The formulation is developed by imposing axisymmetric approximations on the three dimensional formulation described earlier. The current density  $\mathbf{J}$  and magnetic potential  $\mathbf{A}$  are defined as having only an out-of-plane component  $J_\phi$  and  $A_\phi$  (written for convenience as  $J$  and  $A$ ). To avoid singularities in computation, the variables used in the formulation are the modified magnetic potential ( $A' = A/r$ ), modified radial displacement ( $u' = u/r$ ), and axial displacement ( $w$ ). The magnetic flux density vector ( $\mathbf{B}$ ) and the strain vector ( $\mathbf{S}$ ) are kinematically related to  $A'$ ,  $u'$ , and  $w$  through

$$\mathbf{B} = [B_r, B_z]^T = \left[ -r \frac{\partial A'}{\partial z}, r \frac{\partial A'}{\partial r} + 2A' \right]^T, \quad (35)$$

$$\mathbf{S} = [S_{rr}, S_{zz}, S_{rz}, S_{\phi\phi}]^T = \left[ r \frac{\partial u'}{\partial r} + u', \frac{\partial w}{\partial z}, r \frac{\partial u'}{\partial z} + \frac{\partial w}{\partial r}, u' \right]^T. \quad (36)$$

The corresponding work conjugates (magnetic field  $\mathbf{H}$  and stress  $\mathbf{T}$ ) are related to  $\mathbf{B}$  and  $\mathbf{S}$  through constitutive laws and have the form

$$\mathbf{H} = [H_r, H_z]^T, \quad (37)$$

$$\mathbf{T} = [T_{rr}, T_{zz}, T_{\phi\phi}, T_{rz}]^T. \quad (38)$$

Since Terfenol-D transducers work primarily under axial loading, the main quantity of interest is the axial deformation  $w$ . Thus,  $w$  is solved for in all structurally active domains (i.e., they are 'axially active'). For some components, radial deformation may occur due to the geometry of the transducer. In such components, radial deformation  $u$  is also computed. These components are both 'axially active' and 'radially active'. Domains that are only 'axially active' (such as Terfenol-D) have a reduced stress and strain vector with only two components (axial and in-plane shear). This significantly reduces the computation time for the constitutive model inversion.

The reduced finite element system equations can be obtained by transforming the volume integrals in (1) and (2) via the transformation

$$\int_{V_e} (F) dV = 2\pi \int_{A_e} (rF) dr dz. \quad (39)$$

**Discrete energy-averaged constitutive model for Terfenol-D.** Terfenol-D has eight minima along the  $\langle 111 \rangle$  directions. When energy averaged models such as the Armstrong model [24] or the Discrete Energy Averaged Model (DEAM) [22] are compared with measurements, two major discrepancies are observed. First, these models introduce an unphysical kink in the magnetization and magnetostriction, and secondly, the experimentally observed slow approach to saturation is absent. Chakrabarti and Dapino [25] formulated a modified energy-averaged model by superimposing a weighted global anisotropy energy on the local anisotropy energy and using an implicit definition for the smoothing factors.

The total free energy of a domain close to the  $k^{th}$  easy axis  $\mathbf{c}^k$  is formulated as

$$G^k = \underbrace{w^k G_{A_0}^k + \frac{1}{2} K^k \|\mathbf{m}^k - \mathbf{c}^k\|^2}_{G_A^k} - \underbrace{\mathbf{S}_m^k \cdot \mathbf{T}}_{G_C^k} - \underbrace{\mu_0 M_s \mathbf{m}^k \cdot \mathbf{H}}_{G_Z^k}, \quad (40)$$

where  $G_{A_0}^k$  is the global anisotropy energy and  $w^k$  is an empirical weighting factor which adjusts the anisotropy energy along the  $k^{th}$  easy axis. The expression for the minimum energy orientations remains unchanged from the Galfenol constitutive law as the  $\mathbf{m}$ -dependent portion of the energy is the same. The volume fractions are computed using Boltzmann-type averaging (34), the major difference being that the smoothing factor  $\Omega$  is defined as a function of the deviation of the anhysteretic domain volume fractions  $\xi_{an}$  from a homogeneous distribution  $\bar{\xi}$  as

$$\Omega = a_0 + a_1 \|\xi_{an} - \bar{\xi}\|^2. \quad (41)$$

This implicit definition for  $\Omega$  implies that the smoothing factor increases as the domain distribution moves farther away from a homogeneous distribution. This enables the model to describe the slow approach to saturation in Terfenol-D magnetostriction. However, the implicit relationship demands a suitable iterative solution scheme to converge to consistent values of  $\Omega$  and  $\xi_{an}$  which satisfy (34) and (41) simultaneously. In this work, (34) and (41) are combined to form a single scalar equation which is solved using Newton-Raphson iterations. Figure 4 shows the performance of the model in describing the measurements presented by Moffett et al. [26].

**Case study: Terfenol-D engine mount actuator.** The Terfenol-D engine mount actuator also known as the magneto-hydraulic actuator (MHA) consists of a fluid chamber with a large diameter piston at one end driven by a Terfenol-D rod and a small diameter driven piston at the other end (Figure 5).

The magnetic circuit consists of a permanent magnet to provide magnetic bias, a coil to generate the dynamic fields with Terfenol-D at its core, and iron pieces for flux return. Figure 6 shows the 2D axisymmetric version used for modeling. Some components like the stainless steel body and the preload plate have not been modeled as they only serve a geometrical purpose. The device is surrounded by air so that the magnetic potential boundary condition can be applied to the outer boundary of air. In general, flux density measurements are taken by winding a pick-up coil around the middle of the rod and strain measurements are taken by bonding a strain gage close to the midpoint of the rod. Breaking the magnetostrictive rod domain into three parts allows us to evaluate the variables in the central region separately and compare the behavior of the model against measurements. In this actuator, all components are considered to be 'magnetically active' meaning that the magnetic degree of freedom ( $A$ ) is calculated in all the domains. Of these, the base plate, Terfenol-D rod, end caps, pistons, and casing are considered to be structurally active also which means that the mechanical degrees of freedom are calculated in only these components. This partitioning of the solution domain reduces the total degrees of freedom in the model thus shortening the solution time. We now describe the additional physics that was combined with the finite element model to describe the fluid-structure interaction and friction at the fluid seals.

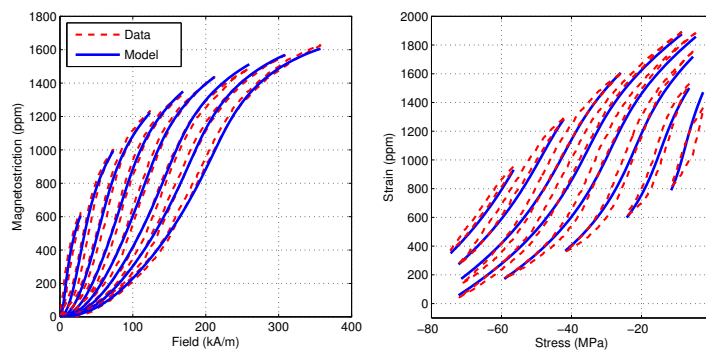


Fig. 4: Comparison of the proposed anhysteretic energy averaged model with measurements by Moffett et al. [26]. All calculated curves have been obtained with the same set of model parameters.

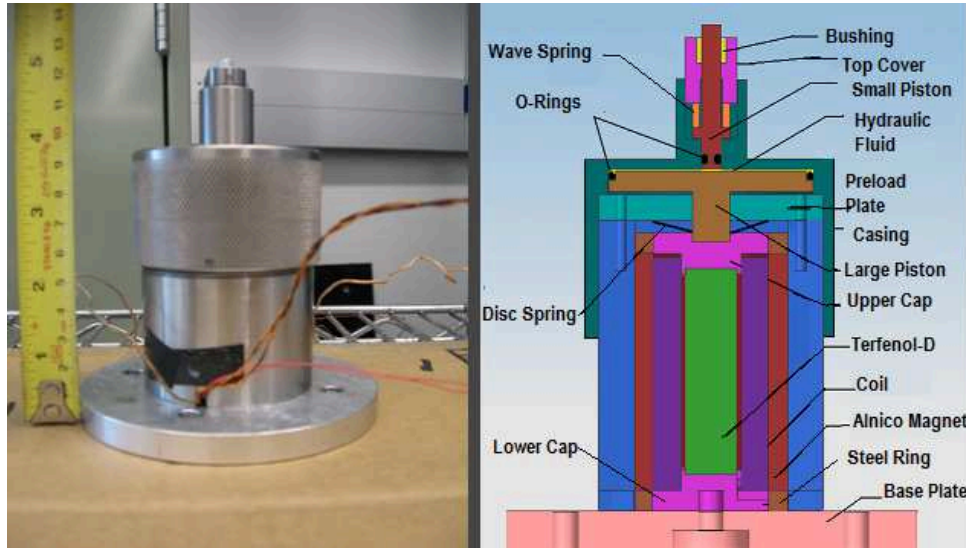


Fig. 5: Physical magneto-hydraulic actuator (left) and cutout (right).

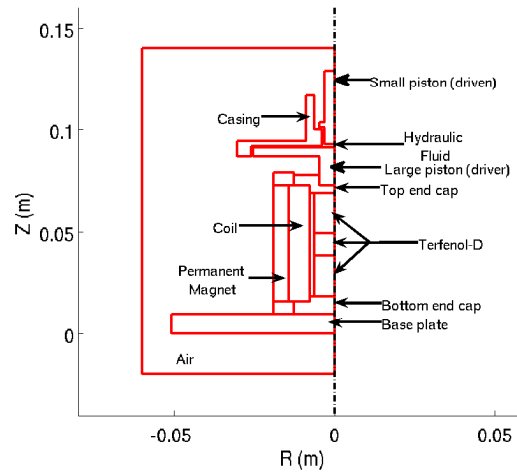


Fig. 6: Geometry of the transducer used in this study.

*Fluid-structure coupling.* Due to the extremely small volume of fluid used in the actuator, inertial effects in the fluid have been neglected. Also, since the seal friction forces are much higher compared to viscous forces in the fluid, damping in the fluid is assumed to be negligible. Thus, only fluid compliance is modeled. The change in volume of the fluid domain  $\Delta V_f$  can be written as a sum of contributions from the drive piston  $\Delta V_P$ , the driven piston  $\Delta V_L$ , and the casing  $\Delta V_C$  as

$$\Delta V_f = -\Delta V_P + \Delta V_L + \Delta V_C, \quad (42)$$

where each of these volume changes are calculated using the integral

$$\Delta V_i = \int_{l_i} 2\pi r w dr, \quad (43)$$

over the length of the edge  $l_i$  exposed to the fluid domain. The pressure change in the fluid is

$$\Delta p = -\frac{\beta}{V_{ref}} \Delta V_f, \quad (44)$$

which is coupled to the structural model through traction on the edges exposed to the fluid. The model describes the effect of compliance of the fluid chamber components. Here,  $\beta$  is the effective bulk modulus of the fluid, while in a previous lumped parameter model [5],  $\beta_{eff}$  represented an effective modulus describing the combined compliance of the fluid and fluid chamber components.

*Seal friction.* Friction forces are present at the o-ring seals in the two pistons. At the smaller (driven) piston seal, actuation forces are low and velocities are high. Hence, even a small friction force at this seal has a significant impact on the dynamic performance of the actuator. On the other hand, at the larger (drive) piston, actuation forces are high and velocities are low. Hence a small frictional force at this end does not affect the dynamic response of the actuator. Thus, friction has been modeled only at the smaller piston seal.

In the LuGre model [27], friction between two sliding surfaces in contact is described as an interaction force between microscopic bristles on both surfaces. The bristle deflection state  $Z_L$  is governed by a nonlinear first-order differential equation,

$$\dot{Z}_L + \sigma_0 \frac{|v_L|}{g(v_L)} Z_L - v_L = 0, \quad (45)$$

where  $v_L$  is the relative sliding velocity between the two surfaces, which in this case is the average velocity of the driven piston calculated by integrating  $2\pi r \dot{w}$  over the edge of the piston adjacent to the casing, divided by the area of that surface. Function  $g(v_L)$  is given by

$$g(v_L) = F_c + (F_s - F_c) e^{-(v_L/v_s)^2}, \quad (46)$$

where  $F_s$  and  $F_c$  are the static and Coulomb friction forces and  $v_s$  is the Stribeck velocity. The friction force is given by

$$F R_L = \sigma_0 Z_L + \sigma_1 \dot{Z}_L + \sigma_2 v_L, \quad (47)$$

where  $\sigma_0$  and  $\sigma_1$  are the bristle stiffness and bristle damping coefficient, respectively. This force is applied as traction on the boundary of the smaller piston adjacent to the casing.

*Boundary conditions.* Boundary conditions for an axisymmetric problem must be implemented carefully such that none of the variables become infinite at the  $r = 0$  boundary. In this case, the axial symmetry condition is enforced using  $(\partial A / \partial r)_{(r=0)} = 0$  in the magnetically active domains,  $u_{(r=0)} = 0$  in the radially active domains, and  $(\partial w / \partial r)_{(r=0)} = 0$  in the axially active domains. These conditions remove shear stresses and constrain the radial displacement at the  $r = 0$  boundary. The magnetostrictive system is encapsulated by a large volume of air. At the outer boundaries of this air volume, the magnetic potential is set to zero. The bottom face of the base plate and the casing are considered to be mechanically fixed.

*Obtaining the bias point.* Computation of the dynamic response of the actuator requires accurate determination of its bias point. The actuator is biased both mechanically and magnetically. The mechanical bias is due to the compression of the wave spring whose force is transmitted (and amplified) through the fluid to the Terfenol-D rod. The stress developed in the Terfenol-D under an axial load can be assumed to be uniform. Therefore, this stress is superimposed directly on the applied stress in the constitutive model. The magnetic bias is due to the residual flux density in the permanent magnet. This field depends on the geometry of the magnetic circuit and cannot be assumed to be homogeneously distributed in the rod. The magnetic bias point is obtained by increasing the residual flux density of the magnet from zero to its actual value using a hyperbolic tangent function and storing the solution from the final step. Figure 7 shows that the axial magnetic field at the bias point is uniformly distributed in the central region of the rod with a somewhat lower value at the ends. The average magnetic field in the Terfenol-D rod is  $\approx 30$  kA/m.

*Response to harmonic inputs.* Figure 8 shows the actuator response at 20, 50, 100, and 200 Hz. As expected the phase between voltage and displacement increases with increasing frequency resulting in counter-clockwise rotation of the loops. One shortcoming of the model is the assumed anhysteretic Terfenol-D behavior which causes a discrepancy in the phase of the response. At lower frequencies this is not visible but at 200 Hz the phase difference is significant.

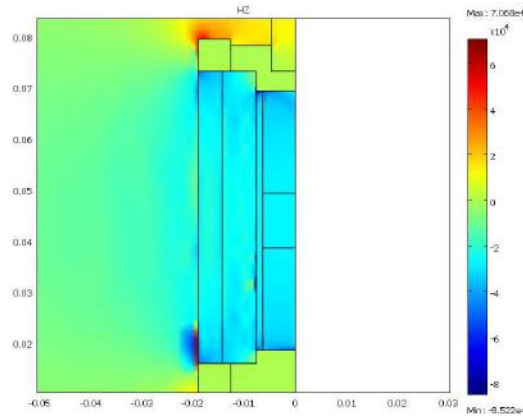


Fig. 7: Axial magnetic field distribution in the magnetic circuit due to the permanent magnet.

An interesting feature that is observed in both the experimental and modeled voltage-current loops is that the actuator draws a biased current even though it is driven with an unbiased sinusoidal voltage input. This happens because of the nonlinear behavior of Terfenol-D. Because the permeability of the material is field-dependent, the back emf in the coil also varies with voltage giving rise to an asymmetric current signal. Such effects can only be described accurately with models where electromagnetic and mechanical responses are fully coupled.

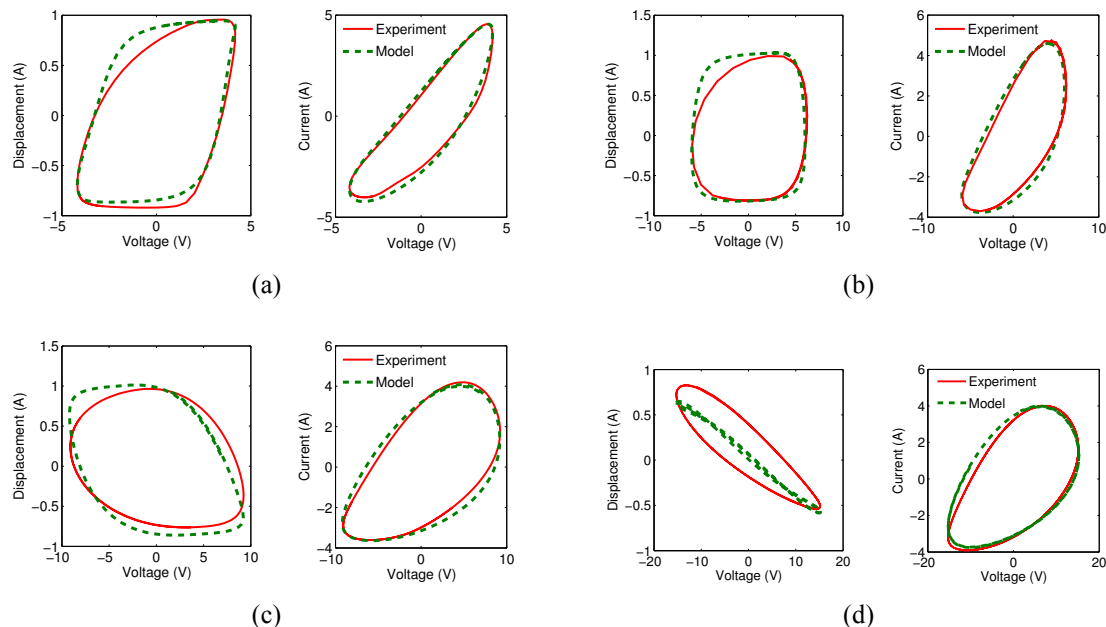


Fig. 8: Comparison of modeled voltage-displacement and voltage-current loops with measurements. (a) 20 Hz, (b) 50 Hz, (c) 100 Hz, and (d) 200 Hz.

*Parametric Study.* The proposed finite element model can be a useful tool for optimizing device geometry and material selection. To illustrate, the effect of fluid bulk modulus, thickness of the fluid chamber components, and seal friction force on the unloaded displacement response of the actuator are studied at 20, 50, 100 and 200 Hz. The effective fluid bulk modulus can have a significant effect on the dynamic performance of hydraulic devices. To investigate the effect of stiffening up the fluid (by degassing), the model is run for  $\beta = 2\beta_0$  and  $\beta = 4\beta_0$ , where  $\beta_0$  is the bulk modulus value tuned to describe the actuator behavior. Figure 9 shows that increasing the bulk modulus four times achieves a mere 2 to 3% increase in the unloaded stroke of the actuator below 100 Hz while a more noticeable 8.5 % increase is observed at 200 Hz. This weak dependence of the actuator performance on the fluid bulk modulus suggests that the performance of the MHA is limited by structural compliance and not the fluid compliance, which is very low as a small volume of fluid is used ( $\approx 1.3$  c.c).

Next, the effect of structural compliance of the fluid chamber components on transducer performance is investigated. The model is run with the thickness of the larger piston and the casing doubled. A significant 30 to 35% stroke increase is estimated in the 20 to 100 Hz range while a large 143% increase is obtained at 200 Hz. Thus, it is concluded that the primary source of compliance in the transducer comes from the components enclosing the fluid.

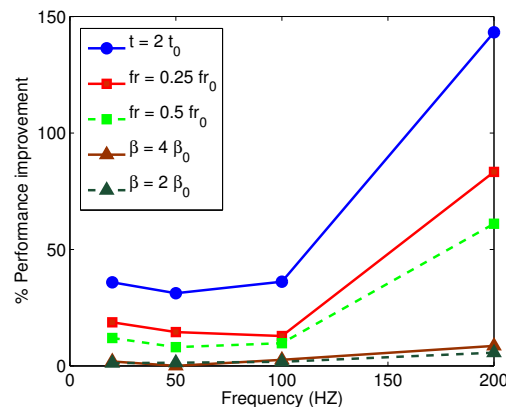


Fig. 9: Percentage improvement in the unloaded stroke of the actuator with variation in model parameters.

Another factor which influences the performance of hydraulic devices is seal friction. The friction force at the smaller piston seal is reduced to  $fr = 0.5 fr_0$  and  $fr = 0.25 fr_0$  where  $fr_0$  is the friction force value tuned to describe the experimentally observed transducer behavior. With the friction force reduced by half, the stroke increases by 10 to 12% in the 20 to 100 Hz range while a 60% increase is calculated at 200 Hz. With the friction force reduced to one fourth of the original value, a 15 to 20% stroke increase is calculated below 100 Hz and a substantial 85% increase is observed at 200 Hz. Thus, as expected, reduction in seal friction can significantly improve the unloaded stroke of the actuator.

## Concluding Remarks

Magnetostrictive materials possess the potential to be applied in novel three dimensional sensors and actuators. Efficient design of such transducers requires an adequate modeling framework which fully describes the nonlinear electro-magneto-mechanical coupling exhibited by these devices. This paper addressed the development of a unified finite element tool whose application is not restricted to a particular magnetostrictive material or transducer configuration. The framework allows for incorporation of any nonlinear constitutive behavior and is able to simultaneously model the effects of structural dynamics, eddy currents, flux leakages and transducer geometry changes on the response of the system. The unified concepts were extended to model transducers employing the two most common magnetostrictive materials: Galfenol and Terfenol-D. For Galfenol, a discrete energy averaged model was

employed with minor refinements to ensure stability in saturation regimes, while for Terfenol-D a modified energy-averaged model with an implicit volume fraction definition was incorporated into a reduced 2D axisymmetric formulation to take advantage of axisymmetric geometries of Terfenol-D actuators. Model results were validated with experiments conducted on a Galfenol unimorph actuator and a Terfenol-D engine mount actuator. The model accurately describes the transient dynamic tip deflection of the unimorph. Results for the Terfenol-D actuator show that the model can describe the steady state dynamic response of the device below 200 Hz. At higher frequencies there are phase errors since hysteretic Terfenol-D material behavior is approximated by an anhysteretic constitutive law. Finally, a parametric study on the mount actuator illustrates the use of this model as a design optimization tool. Significant improvements can be obtained in the unloaded stroke of the actuator by increasing the thickness of the components enclosing the fluid and reducing seal friction.

### Acknowledgements

Financial support for this research was provided by the Smart Vehicle Concepts Center, a National Science Foundation Industry/University Cooperative Research Center ([www.SmartVehicleCenter.org](http://www.SmartVehicleCenter.org)), and by the ONR MURI Grant # N000140610530 (Jan Lindberg program manager).

### References

- [1] M.J. Dapino, "On magnetostrictive materials and their use in adaptive structures," *Structural Engineering and Mechanics*, Vol. 17, No. 3-4, pp. 303-329, 2004.
- [2] Huang, W., Wang, B., Cao, S., Sun, Y., Weng, L., and Chen, H., "Dynamic strain model with eddy current effects for giant magnetostrictive transducer," *IEEE Transactions on Magnetics* **43**, 1381--1384 (April 2007).
- [3] Jiles, D., "Modeling the effects of eddy current losses on frequency dependent hysteresis loops in electrically conducting media," *IEEE Transactions on Magnetics* **30**(6), 4326--4328 (1994).
- [4] Sarawate, N. and Dapino, M., "A dynamic actuation model for magnetostrictive materials," *Smart Materials and Structures* **17**, 065013 (2008).
- [5] Chakrabarti, S. and Dapino, M., "A dynamic model for a displacement amplified magnetostrictive driver for active mounts," *Smart Materials and Structures* **19**, 055009 (2010).
- [6] Evans, P., *Nonlinear magnetomechanical modeling and characterization of Galfenol and system-level modeling of Galfenol-based transducers*, PhD thesis, The Ohio State University (2009).
- [7] Benbouzid, M., Beguenane, R., Reyne, G., and Meunier, G., "Finite element modeling of Terfenol-D magneto-mechanical coupling: application to a direct micro-stepping rotary motor," (1997).
- [8] Kannan, K. and Dasgupta, A., "A nonlinear Galerkin finite-element theory for modeling magnetostrictive smart structures," *Smart Materials and Structures* **6**, 341--350 (1997).
- [9] Zhou, H. and Zhou, Y., "Vibration suppression of laminated composite beams using actuators of giant magnetostrictive materials," *Smart materials and structures* **16**, 198--206 (2007).
- [10] Zheng, X. and Liu, X., "A nonlinear constitutive model for Terfenol-D rods," *Journal of applied physics* **97**(5), 053901 (2005).

- [11] Kim, J. and Jung, E., "Finite element analysis for acoustic characteristics of a magnetostrictive transducer," *Smart Materials and Structures* **14**, 1273--1280 (2005).
- [12] Ghosh, D. and Gopalakrishnan, S., "Coupled analysis of composite laminate with embedded magnetostrictive patches," *Smart Materials and Structures* **14**, 1462 (2005).
- [13] Pérez-Aparicio, J. and Sosa, H., "A continuum three-dimensional, fully coupled, dynamic, non-linear finite element formulation for magnetostrictive materials," *Smart Materials and Structures* **13**, 493--502 (2004).
- [14] Slaughter, J., "Coupled structural and magnetic models: linear magnetostriction in COMSOL," *Proceedings of COMSOL Conference* (2009).
- [15] Mudivartha, C., Datta, S., Atulasimha, J., and Flatau, A., "A bidirectionally coupled magnetoelastic model and its validation using a Galfenol unimorph sensor," *Smart Materials and Structures* **17** (2008).
- [16] Graham, F., Mudivartha, C., Datta, S., and Flatau, A., "Modeling of a Galfenol transducer using the bidirectionally coupled magnetoelastic model," *Smart Materials and Structures* **18**, 104013 (2009).
- [17] Armstrong, W., "Magnetization and magnetostriction processes in  $\text{Tb}_{0.27-0.30}\text{Dy}_{0.73-0.70}\text{Fe}_{1.9-2.0}$ ," *Journal of Applied Physics* **81**(5), 2321--2326 (1997).
- [18] Evans, P. and Dapino, M., "Dynamic Model for 3-D Magnetostrictive Transducers," *Magnetics, IEEE Transactions on* **47**(1), 221--230 (2011).
- [19] Benbouzid, M., Reyne, G., Meunier, G., Kvarnsjo, L., and Engdahl, G., "Dynamic modelling of giant magnetostriction in Terfenol-D rods by the finite element method," *Magnetics, IEEE Transactions on* **31**(3), 1821--1824 (1995).
- [20] Bathe, K., [*Finite Element Procedures*], Prentice Hall, Upper Saddle River, New Jersey 07458 (1996).
- [21] Atulasimha, J., Akhras, G., and Flatau, A., "Comprehensive 3-d hysteretic magnetomechanical model and its validation with experimental  $\langle 110 \rangle$  single-crystal iron-gallium behavior," *Journal of Applied Physics* **103**, 07--336 (2008).
- [22] Evans, P. G. and Dapino, M. J., "Efficient magnetic hysteresis model for field and stress application in magnetostrictive Galfenol," *Journal of Applied Physics* **107**(6), 063906 (2010).
- [23] Chakrabarti, S. and Dapino, M. J., "Nonlinear finite element model for 3D Galfenol systems," *Smart Materials and Structures* **20**(10), 105034 (2011).
- [24] Armstrong, W. D., "An incremental theory of magneto-elastic hysteresis in pseudo-cubic ferromagnetostrictive alloys," *Journal of Magnetism and Magnetic Materials* **263**, 208 (2003).
- [25] Chakrabarti, S. and Dapino, M. J., "Fully coupled discrete energy-averaged model for Terfenol-D," *Journal of Applied Physics* **111**(5), 054505 (2012).
- [26] Moffett, M., Clark, A., Wun-Fogle, M., Linberg, J., Teter, J., and McLaughlin, E., "Characterization of Terfenol-D for magnetostrictive transducers," *The Journal of the Acoustical Society of America* **89**, 1448 (1991).
- [27] Olsson, H., Astrom, K. J., de Wit, C. C., Gafvert, M., and Lischinsky, P., "Friction models and friction compensation," *Eur. J. Control* **4**(3), 176--195 (1998).